REALISTIC SOLAR CONVECTION SIMULATIONS

ROBERT F. STEIN[1] and ÅKE NORDLUND[2]
[1]*Michigan State University, East Lansing, MI 48824, U.S.A.*
[2]*Theoretical Astrophysics Center and Astronomical Observatory/NBIfAFG, Juliane Maries Vej 30, Dk-2100 Copenhagen Ø, Denmark*

(Received 4 October 1999; accepted 6 January 2000)

Abstract. We report on realistic simulations of solar surface convection that are essentially parameter-free, but include detailed physics in the equation of state and radiative energy exchange. The simulation results are compared quantitatively with observations. Excellent agreement is obtained for the distribution of the emergent continuum intensity, the profiles of weak photospheric lines, the p-mode frequencies, the asymmetrical shape of the mode velocity and intensity spectra, the p-mode excitation rate, and the depth of the convection zone. We describe how solar convection is non-local. It is driven from a thin surface thermal boundary layer where radiative cooling produces low entropy gas which forms the cores of the downdrafts in which most of the buoyancy work occurs. Turbulence and vorticity are mostly confined to the intergranular lanes and underlying downdrafts. Finally, we present some preliminary results on magneto-convection.

1. Introduction

Convection is inherently three-dimensional, non-linear and non-local. Hence, it is best studied using computational fluid dynamic simulations. Two complementary approaches using numerical simulations have both contributed toward understanding convection. One uses simplified physics to explore the basic properties of convection and the deep solar convection zone (e.g., Chan and Sofia, 1989; Cattaneo *et al.*, 1991; Porter and Woodward, 1994; Brummell, Hurlburt, and Toomre, 1996; Hurlburt, Matthews, and Proctor, 1996; Weiss *et al.*, 1996; Elliott *et al.*, 1998; Cattaneo, 1999). The other approach uses realistic physics to make quantitative predictions to compare with solar and stellar observations and explore physical processes in the upper solar convection zone (e.g., Nordlund, 1985; Freytag, Ludwig, and Steffen, 1996; Stein and Nordlund, 1998; Rosenthal *et al.*, 1998). We have chosen this latter approach. We briefly describe our numerical method, compare the predictions from the simulations with observations and present a few basic conclusions about the nature of solar and stellar convection.

2. Numerical Method

We model convection using a three-dimensional, compressible, MHD code to integrate the conservation equations for mass, momentum and internal energy and

Solar Physics **192:** 91–108, 2000.

the induction equation for the vector potential. The equations are written in non-conservative form, using the variables: log density, $\ln \rho$, velocity, $\mathbf{u}$, internal energy per unit mass, e, and vector potential, $\mathbf{A}$, which are all defined at the same grid locations:

$$\frac{\partial \ln \rho}{\partial t} = -\mathbf{u} \cdot \nabla \ln \rho - \nabla \cdot \mathbf{u} \,, \tag{1}$$

$$\frac{\partial \mathbf{u}}{\partial t} = -\mathbf{u} \cdot \nabla \mathbf{u} + \mathbf{g} - \frac{P}{\rho} \nabla \ln P + \frac{1}{\rho} \mathbf{J} \times \mathbf{B} + \frac{1}{\rho} \nabla \cdot \tau \,, \tag{2}$$

$$\frac{\partial e}{\partial t} = -\mathbf{u} \cdot \nabla e - \frac{P}{\rho} \nabla \cdot \mathbf{u} + Q_{\text{rad}} + Q_{\text{visc}} + Q_{\text{joule}} \,, \tag{3}$$

$$\frac{\partial \mathbf{A}}{\partial t} = \mathbf{u} \times \mathbf{B} - \eta \mathbf{J} \tag{4}$$

(Nordlund and Stein, 1989, 1990). Here $\mathbf{g}$ is the gravitational acceleration, P is the gas pressure, $\mathbf{J}$ is the electric current density, $\mathbf{B}$ is the magnetic field, τ is the viscous stress tensor, Q_{rad} is the radiative heating, Q_{visc} and Q_{joule} are the viscous and resistive dissipation respectively, and η is the resistivity. The time advance is a third order leapfrog predictor-corrector (Hyman, 1979). Spatial derivatives are calculated using sixth-order compact derivatives in the horizontal directions and cubic splines in the vertical direction, to achieve high accuracy with small numerical damping. We use logarithmic variables to increase the accuracy of the hydrostatic balance.

The only parameters in the simulation are the numerical resolution and the numerical viscosity coefficients. Our highest resolution is $253 \times 253 \times 163$ deep covering a computational domain 6×6 Mm horizontally and extending from the temperature minimum down to 2.5 Mm below the visible surface. Sufficient numerical diffusion is introduced into each equation to prevent the buildup of energy at the smallest scales and stabilize the code (Rogallo and Moin, 1984; Boris, 1989; Porter *et al.*, 1992). To avoid unphysically damping the well resolved scales we use a hyperviscosity diffusion algorithm in which diffusion decreases rapidly with increasing wavelength. The numerical viscosity coefficients are chosen as the minimum needed to keep all the variables varying smoothly.

The calculations include enough detailed physics to realistically model convection near the solar surface and the overlying photosphere. An appropriate equation of state and accurate radiative energy exchange are crucial physical effects that must be included in order to make quantitative comparisons with solar observations.

Ionization dominates the internal energy near the surface. Figure 1 shows the fluxes of the different forms of energy. The ionization energy flux is 3 times larger than the thermal energy flux and accounts for $\frac{2}{3}$ of the total enthalpy flux. Since the net flux is constrained to equal the solar value, in order to reproduce the solar

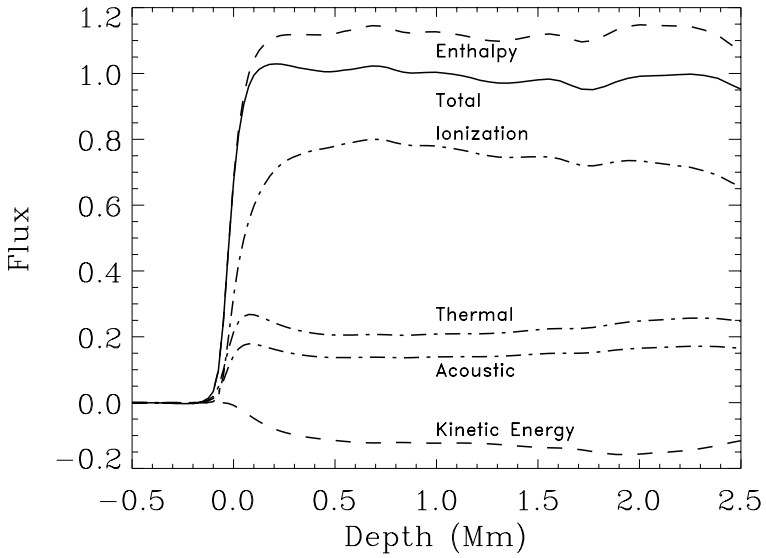

Figure 1. Energy flux and its contributions. The dominant flux is of the hydrogen ionization energy. At the surface, the energy flux becomes entirely radiative (not shown).

temperature and velocity fluctuation amplitudes it is necessary to include the ionization energy contribution to the flux. We therefore use a tabular equation of state that includes ionization and excitation of hydrogen, helium and other abundant atoms, and formation of H_2 molecules.

Radiative energy exchange plays a crucial role in determining the structure of the upper convection zone. It determines what we observe and generates the entropy fluctuations that produce the buoyancy work which drives the convection. Since the top of the convection zone occurs near the level where the continuum optical depth is one, neither the optically thin nor the diffusion approximations give reasonable results. We therefore include 3-D, LTE radiation transfer in our model. The radiative energy exchange rate is found by solving the Feautrier equation along straight, slanted, rays, after averaging the Planck function into four bins by wavelength sorted according to opacity (cf., Nordlund, 1982; Nordlund and Stein, 1990, 1991). Line blocking modifies the atmospheric structure by increasing the photospheric temperature and must also be included.

Boundary conditions control how the fluid behaves in accordance with the conservation laws. The boundaries of our computational domain are ‘virtual boundaries’. The region we simulate is, in reality, coupled to an external medium, about which we have no a priori information. However, convection is driven by entropy fluctuations generated near the surface by radiative cooling. Deeper layers asymptotically approach an adiabatic mean state, in which ascending gas is nearly isentropic and uniform. For this reason, the lack of information about the region below our model is not likely to be a significant source of uncertainty. The re-

gion above our model contains too little mass to be able to significantly influence the interior. To minimize the effects of the boundaries we use periodic horizontal boundary conditions and transmitting top and bottom boundary conditions. To peg conditions at their solar values we specify the entropy of the incoming fluid at the bottom. For stability, the total pressure (gas + magnetic) is made horizontally uniform by adjusting the mass and energy densities consistent with isentropy. The magnetic field is assumed to be potential at the top and several different bottom boundary conditions are used to mimic different physical situations – vertical field or specified horizontal field in the inflow. To facilitate the analysis of p-mode driving we also make the bottom a node for vertical modes by imposing the condition that the instantaneous net vertical mass flux is zero.

3. Simulation vs. Observations

The simulation results can be directly compared with solar observations. We have compared the properties of the granulation, the profiles of weak photospheric lines, the frequencies of the p modes, the p-mode spectrum asymmetries, the rate of p-mode excitation and the depth of the convection zone. The excellent agreement found for these many different diagnostics validates the simulations and gives us the confidence needed to use them to investigate properties of solar convection that are not directly observable. The remaining discrepancies point the way to further studies that need to be performed.

3.1. GRANULATION

Emergent radiation from the solar surface can be resolved spatially and temporally. Hence, direct comparison can be made between the simulated and observed granulation (Figure 2). Raw images of the emergent intensity from the simulation with a horizontal resolution of 25 km show more detail than is visible in even the best observations of solar granulation (cf. Figure 2 top and bottom panels). The raw images have an rms intensity fluctuation of order 20%. Folding the image with the appropriate point spread function to take account of the telescope resolution and atmospheric seeing (middle panel) reduces this to the observed value, $\approx 10\%$.

Quantitative comparison can be made between the observed and calculated granulation properties. The size spectrum of the granulation matches well (Figure 3(a)) and reflects primarily the sharpness of the edges of the granules. The probability density function of the emergent radiation also agrees closely with observed granulation (Figure 3(b)).

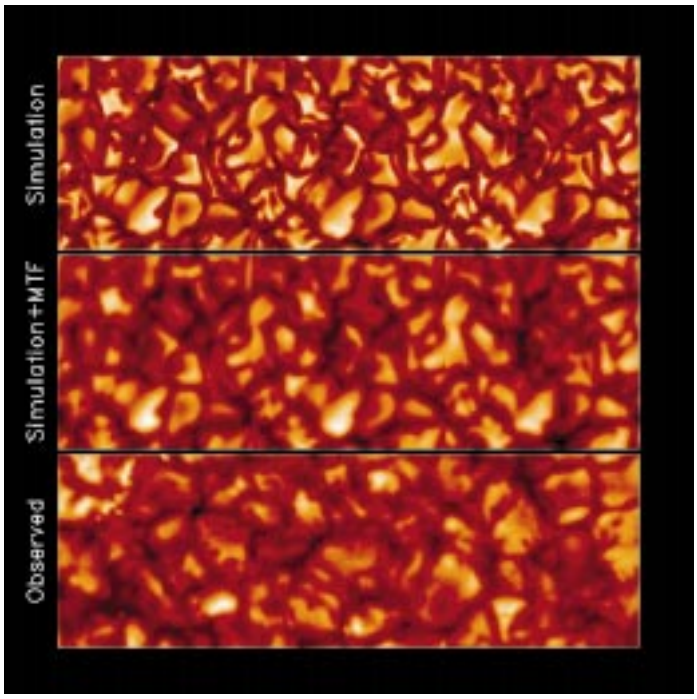

Figure 2. Emergent continuum radiation (granulation) from the simulation with 25 km resolution (*top*). Each image is 18×6 Mm. The same image folded with a point spread function for the telescope and atmospheric seeing (*middle*). An image (to the same scale) from the Swedish Solar Telescope at La Palma (*bottom*).

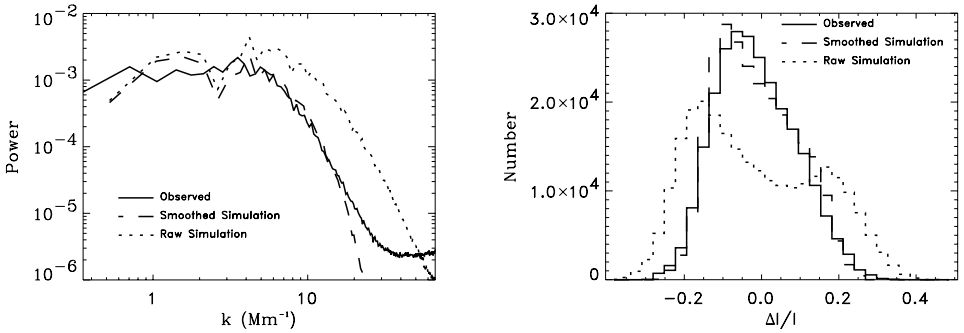

Figure 3. (a) Horizontal size spectrum of observed and simulated granules including effects of smoothing by the point spread function. The simulation intensity smoothed by the appropriate point spread function for the Swedish Solar Telescope on La Palma agrees very closely with the observed spectrum. However, any image with sharp boundaries produces a similar spectrum. Hence, this spectrum only shows that granules have very steep boundaries. (b) Histogram of the emergent radiation intensity from the raw simulation, after smoothing with the psf and from a snapshot of observations made by the Swedish Solar Telescope on La Palma. Note the asymmetric shape and good agreement between the observations and the smoothed simulation.

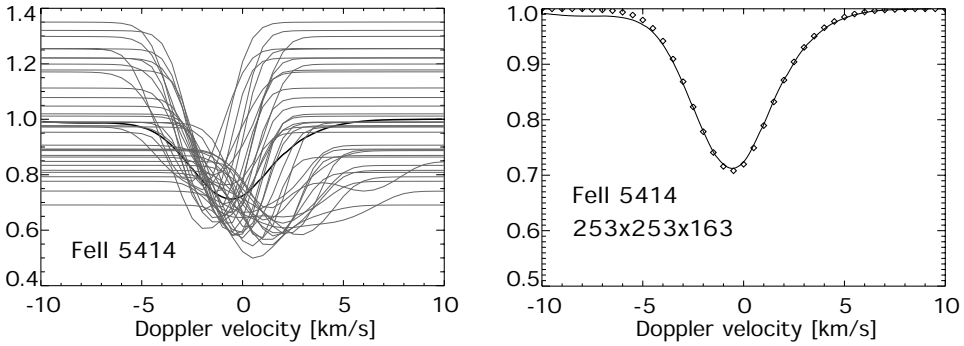

Figure 4. (a) The average emergent line profile is a combination of profiles from different, unresolved, locations on the Sun, each of which has very different shifts, widths and shapes. The thick line is the average profile. The grey lines are from individual horizontal grid points in a snapshot. (b) Comparison of observed (*solid*) and simulated (*diamonds*) Fe II λ5414 line profiles for a $253 \times 253 \times 163$ simulation. The agreement is excellent. FWHM are within 1.5%.

3.2. PHOTOSPHERIC LINE PROFILES

Spectral lines of heavy elements, such as iron, whose thermal Doppler widths are small compared to typical photospheric velocities, provide direct diagnostics of velocity and temperature fluctuations in the photosphere. Non-spatially resolved properties such as average line widths, shape and shifts are useful because they bypass the difficulties associated with atmospheric seeing and instrumental resolution. Line profiles are an average over many spatial locations with different temperatures and line of sight velocities. Line widths test the flow velocities. Line shifts test the correlation between temperature fluctuations and velocity. The profile shape (bisector) tests convective overshooting.

Weak lines (with a small ratio of radiative to collisional rates) are insensitive to non-LTE population effects. Fe II is the dominant ionization stage in the low photosphere, so its lines are insensitive to non-LTE ionization effects. We therefore used weak Fe II lines to compare predicted profiles from the simulation with observations. There are no free parameters (no micro- or macro-turbulence, no enhanced damping). The observed average line profile is the result of spatial and temporal averaging of lines with very different shifts, widths and shapes (Figure 4(a)). With both the simulation temperatures and velocities included there is excellent agreement between the observed and simulated profiles (Figure 4(b)). At the highest spatial resolution of 25 km horizontally and 15–35 km vertically, the FWHM of weak and intermediately strong lines agree with observations to within 1.5%. The 3-D profiles do depend somewhat on the numerical resolution (Figure 5(a)). With the simulation temperature structure, but no velocities, the lines are much too narrow and deep (Figure 5(b)). Two-dimensional simulations do not give the observed profiles.

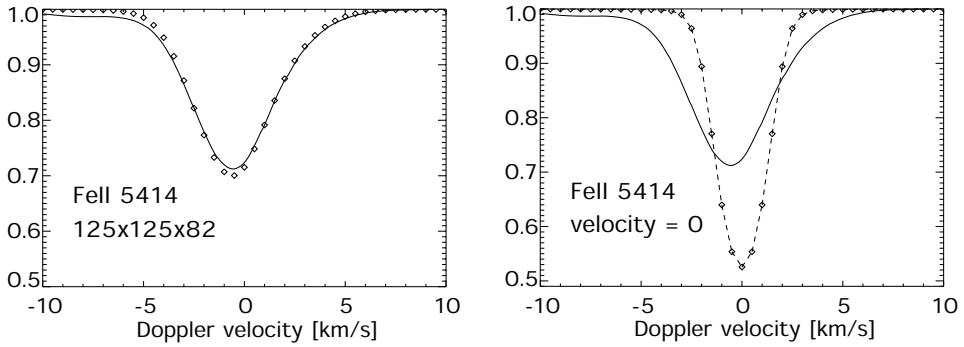

Figure 5. (a) Comparison of observed (*solid*) and simulated (*diamonds*) Fe II λ5414 line profiles for a 125 × 125 × 82 simulation. At this lower resolution the line is slightly too deep and narrow. (b) The weak Fe II line λ5414, as observed (*solid*) and as it would appear if there were no photospheric velocities (*diamonds*).

3.3. *p*-MODE FREQUENCIES

The p-mode eigenfrequencies test the mean envelope structure which determines their resonant cavity. Spherically symmetric models with a mixing length treatment of convection have resonant cavities for high-frequency modes that are too small, yielding theoretical eigenfrequencies that are larger than those observed (Figure 6). The discrepancies increase with increasing frequency, ν, but are independent of degree, ℓ (when scaled by the ratio of the mode mass to the mode mass of a radial mode of the same frequency). Hence, their cause resides in layers to which the low-frequency modes hardly penetrate, but where the high-frequency modes have a significant amplitude. Low-frequency modes have their upper turning point below the highly superadiabatic region near the top of the convection zone. High-frequency modes have their upper turning points above the this layer. Thus, an error exists in the standard models in the super-adiabatic convective boundary layer and above.

Calculating the eigenfrequencies from the horizontally and temporally average structure of our convection simulations (extended by a mixing length envelope model in the adiabatic layers below our computational domain) reduces the discrepancy by a factor of three (Figure 6, Rosenthal *et al.*, 1999). The resonant cavity of the higher frequency modes is enlarged by two effects: (1) Turbulent pressure, which is large only near the superadiabatic layer at the top of the convection zone, elevates the photospheric layers while leaving the region below the superadiabatic layer unchanged (Figure 7(a)). (2) 3-D radiative transfer makes the simulation hotter on average than the corresponding 1-D model that emits the same solar flux. This produces a larger scale height and a more extended atmosphere. The reason is the high temperature sensitivity of the H^- opacity ($\kappa \sim T^{10}$) due to hydrogen ionization producing electrons. The visibility of positive temperature fluctuations (with increased opacity) is reduced, while the visibility of

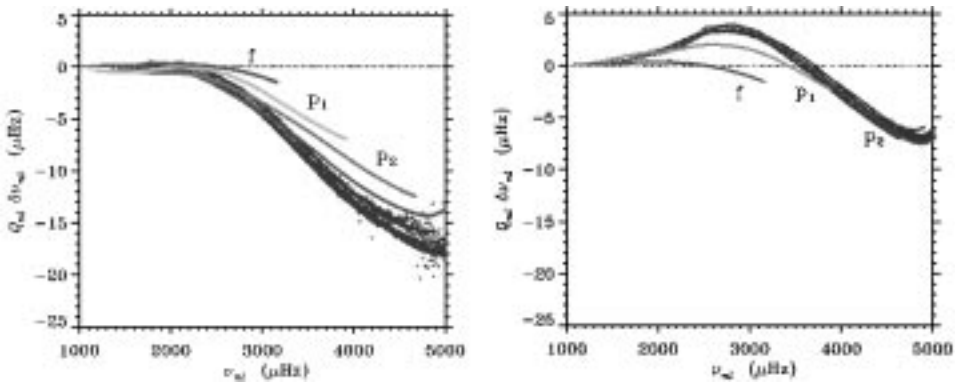

Figure 6. Difference between observed p-mode frequencies and theoretical eigenfrequencies (scaled by the ratio of the mode mass to the mode mass of a radial mode of the same frequency) for a standard 1-D solar model (*left*) and for a horizontally and temporally averaged 3-D model extended downwards by a standard envelope model in the adiabatic layers below the simulation domain (*right*). The 3-D simulation has an elevated photosphere which enlarges the cavity for high-frequency p-modes and reduces their frequency in better agreement with observations.

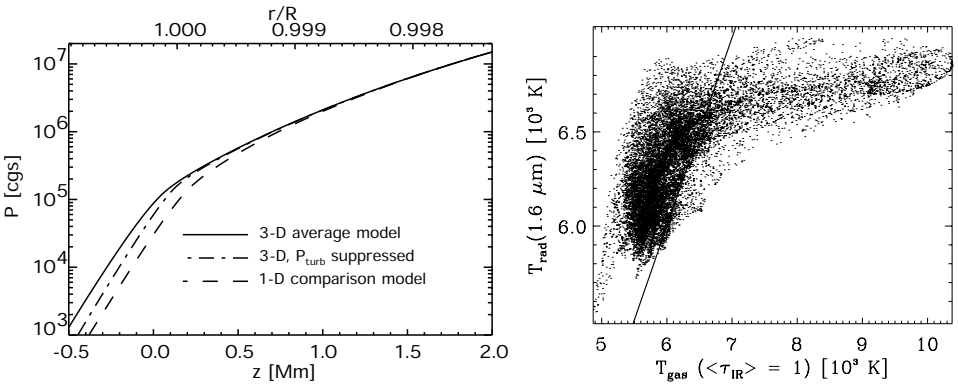

Figure 7. (a) Pressure as a function of depth for an averaged 3-D model (*solid*), for a 3-D model with no turbulent pressure (*dot-dashed*), and for a standard 1-D envelope model (*dashed*). (b) Correlation of radiation temperature of emergent IR radiation and gas temperature at the same horizontal location and $\langle\tau\rangle = 1$. Only cool gas is visible, because of the rapid increase in H^- opacity with temperature.

negative temperature fluctuations (with reduced opacity) is increased (Figure 7(b)). Hence, the emergent radiation in a 3-D model is cooler than a 1-D model with the same average temperature. The elevation of the photosphere extends the cavity of the high-frequency modes, while leaving the cavity of low-frequency modes unchanged. The remaining discrepancies are of the same order of magnitude as that for the fundamental mode, which is insensitive to the atmospheric structure and the adiabatic exponent (Γ_1). They are probably due to non-adiabatic wave propagation in an inhomogeneous 3-D medium.

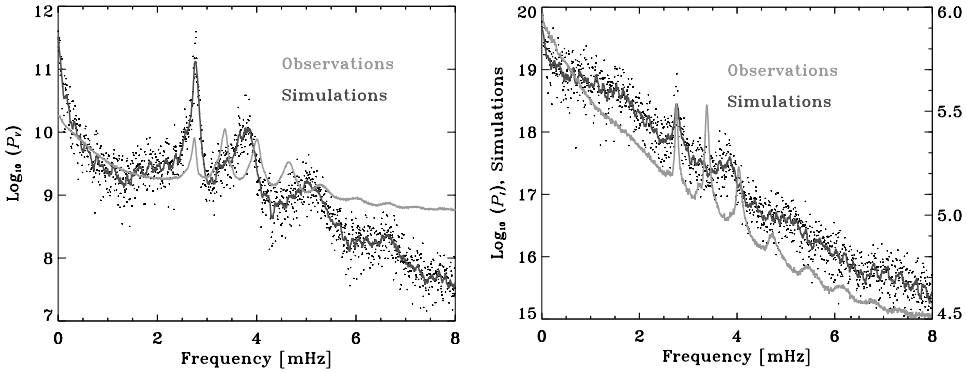

Figure 8. Velocity power spectrum (*left*) and continuum intensity power spectrum (*right*) for the first non-radial modes of the simulation compared with $\ell = 740$ modes observed by SOHO/MDI. The simulation velocity is taken at 200 km above $\langle \tau_{5000} \rangle = 1$. Dots show the raw simulation values and the solid line is the running average.) The asymmetry is similar in both the observed and simulated modes, and the asymmetry is reversed between the velocity and intensity in both the simulations and observations. The lowest frequency mode in both the simulation and observations is the fundamental. Its properties are very similar in both. The higher frequency modes are the p modes. The simulation spectrum has fewer, broader, more widely separated p modes than the observed modes because the computational domain is shallow and the mode mass smaller. Yet the asymmetry properties are similar. The simulation spectrum falls off more rapidly at high frequencies because of its limited resolution.

3.4. p-MODE SPECTRAL ASYMMETRY

The power spectrum of solar acoustic oscillations is asymmetric and the asymmetry is reversed between velocity and intensity, with velocity power being larger on the low-frequency side of a mode and the intensity power being larger on the high frequency side (Duvall *et al.*, 1993; Nigam *et al.*, 1998). The reversal of asymmetry between velocity and intensity is believed to be due to the interaction between the oscillations and correlated noise from the convection (Rast and Bogdan, 1998; Nigam *et al.*, 1998; Kumar and Basu, 1999). This same asymmetry, with the reversal between velocity and intensity, is also found in the modes of our simulation (Figure 8 and Georgobiani *et al.* (2000)).

3.5. p-MODE EXCITATION

The p-mode oscillation excitation rate is another check on the validity of the numerical simulations. The modes are excited by the work of stochastic, non-adiabatic, pressure (entropy) fluctuations (Stein and Nordlund, 1991),

$$W = \int \mathrm{d}t \int \mathrm{d}z \delta P \frac{\partial \dot{\xi}}{\partial z} \,, \tag{5}$$

where δP is the pressure fluctuation and ξ is the displacement. Since this is a stochastic process, the pressure fluctuations occur with random phases with respect

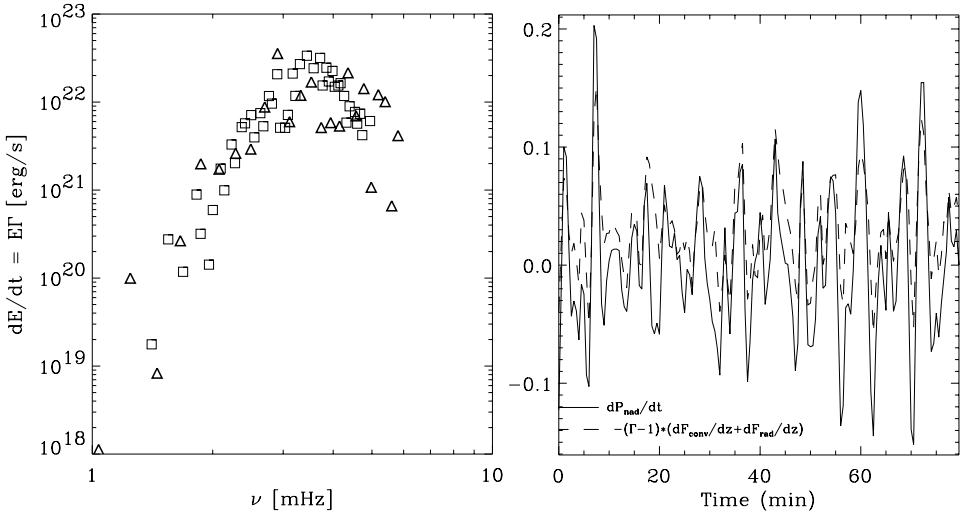

Figure 9. (a) Energy input to modes (simulation = diamonds, observations = squares) from Roca Cortes *et al.* (1999), based on observed mode velocity amplitudes and line widths from GOLF. (b) Non-adiabatic pressure fluctuations are produced by the local, instantaneous imbalance between the divergence of the convective and radiative fluxes. Units are 10^3 erg cm^{-3} s^{-1}. The non-adiabatic pressure fluctuations are due to small instantaneous imbalances between radiative cooling and convective energy supply.

to the modes. Therefore one must average over all possible relative phases between them. The resulting rate of energy input to the modes is (Nordlund and Stein, 1999)

$$\frac{\Delta\langle E_\omega\rangle}{\Delta t} = \frac{\omega^2 \left| \int_r \mathrm{d}r \delta P_\omega^* \frac{\partial \xi_\omega}{\partial z} \right|^2}{8\Delta\nu E_\omega}, \tag{6}$$

where E_ω is the mode energy. Observationally, the excitation rate is determined by measuring the mode amplitudes and line widths.

The simulation and observed mode excitation rates as a function of mode frequency are in good agreement (Figure 9(a)). The pressure fluctuations and the displacement have contributions from both the modes and the convection. The dominant driving comes from the work of the non-adiabatic, stochastic pressure fluctuations, which are produced by small instantaneous local imbalances between the divergence of the radiative and conductive fluxes near the solar surface (Figure 9(b)), acting on the coherent mode displacement. Mode driving (Equation (6)) decreases at low frequency because the mode compression, $\partial\xi_\omega/\partial z$, decreases and the mode energy, E_ω, increases at low frequency (Figure 10(a)). Mode driving decreases at high frequency because the pressure fluctuations, δP_ω, decrease at high frequency (Figure 10(b)).

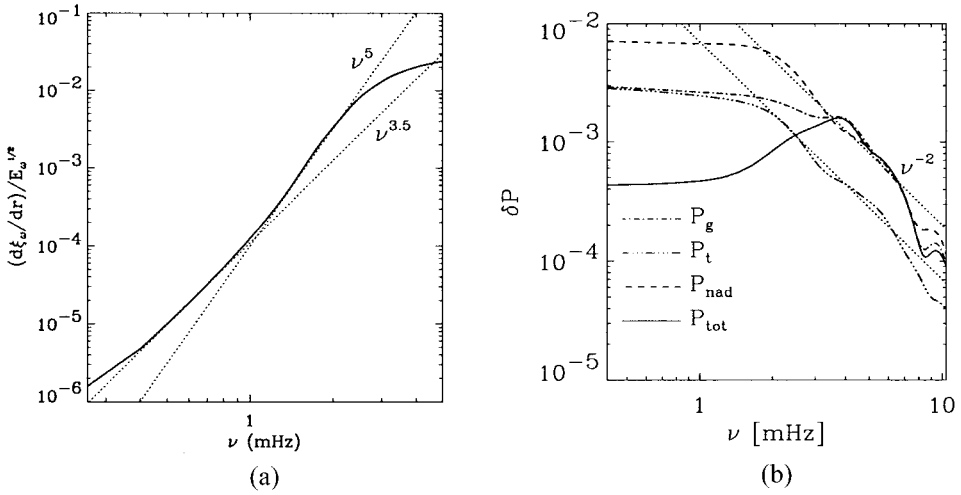

Figure 10. (a) The mode factor in the work integral: $(\partial\xi_\omega/\partial z)/E_\omega^{1/2}$. Excitation decreases at low frequency due to mode behavior. The mode compression decreases with decreasing frequency because the radial wave vector is approximately $k = \omega^2/g$ and the mode mass increases with decreasing frequency. (b) Spectrum of pressure fluctuations. At high frequencies the pressure fluctuations decrease as ν^{-2} and in the peak driving range of 3–4 mHz the non-adiabatic gas pressure fluctuations dominant the pressure fluctuations. P_g is the gas and P_t is the turbulent pressure, $P_{\rm tot}$ is the total (gas + turbulent) pressure fluctuation and $P_{\rm nad}$ its non-adiabatic part. Units are 10^7 dynes cm^{-2} Hz^{-1}.

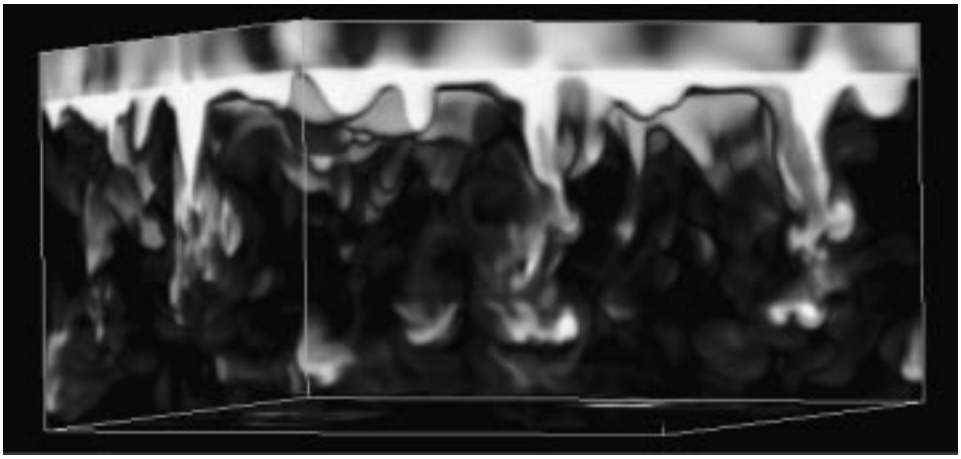

Figure 11. Snapshot of entropy fluctuations. Low entropy gas forms the cores of downdrafts that penetrate through the entire computational domain.

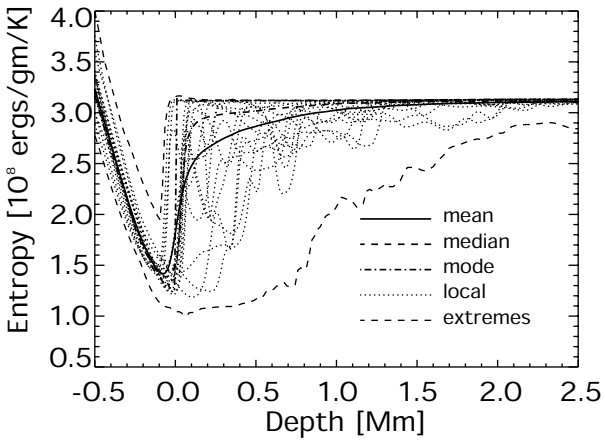

Figure 12. Entropy as a function of depth showing the mean, median, mode, extremes and several individual horizontal locations (*dotted*). Most of the entropy fluctuations below the surface occur in the downdrafts. The upflowing gas all has nearly the same (maximum) entropy. The range of fluctuations decreases with depth due to entrainment, mixing and thermal diffusion.

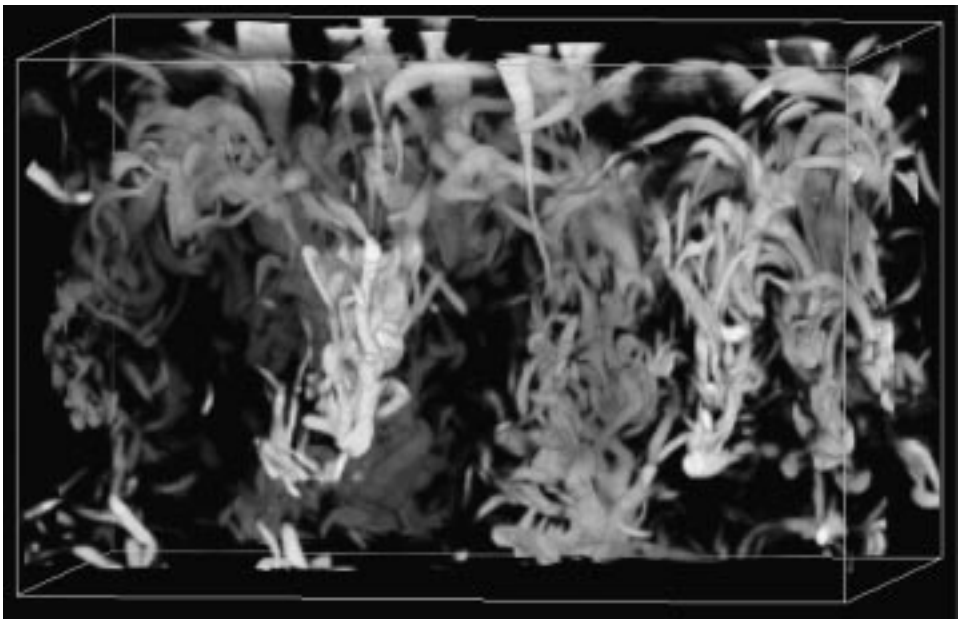

Figure 13. Snapshot of vorticity. Vortex tubes intertwine in the downdrafts illustrating their turbulent nature.

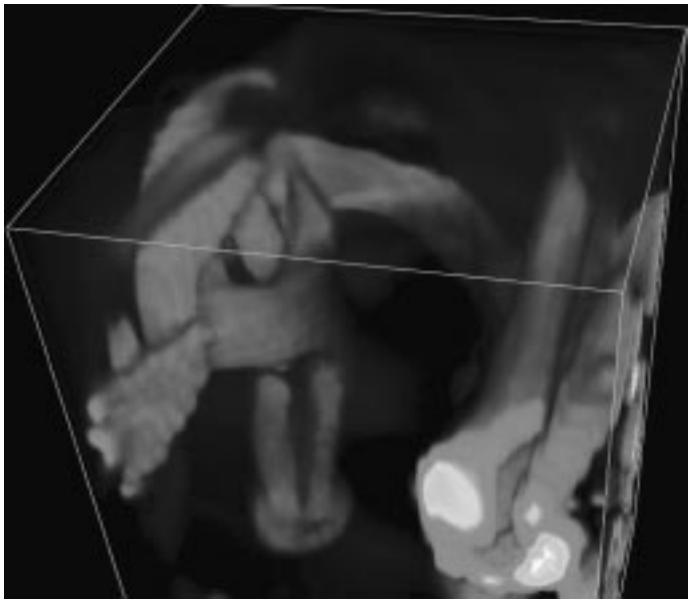

Figure 14. Vortex tubes in a granule. Pairs of horizontal vortex tubes occur at the edges of the intergranular lanes where fluid turns over and begins descending. A ring vortex occurs at the head of a downdraft with a pair of trailing vortex tubes connecting back to the surface.

3.6. DEPTH OF THE CONVECTION ZONE

The depth of the convection zone provides another test of the accuracy of the numerical convection models. The depth depends on: (1) The equation of state, which is fairly well known (Hummer and Mihalas, 1988; Mihalas, Däppen, and Hummer, 1988; Däppen *et al.*, 1988; Mihalas *et al.*, 1990). (2) The entropy jump in the superadiabatic layer just below the surface, which in turn depends on the details of the treatment of convection. (3) The temperature structure of the surface layers. Spectral line blocking raises the solar surface temperature by about 3% (170 K) and also must be taken into account. Helioseismology gives the depth as 0.287 $R_\odot$ (Basu and Antia, 1997). The convection zone depth inferred from the horizontal and temporal average of our 3-D simulations extended down with a mixing length envelope model in the adiabatic regions below the bottom of the computational domain (temperature 20 000 K, depth 2.5 Mm) is 0.286 $R_\odot$ (Rosenthal *et al.*, 1999).

4. Solar Convection

The agreement between the simulation and a variety of observations, which are sensitive to different properties of convection, gives us confidence to use the simulations to understand non-observable convective properties.

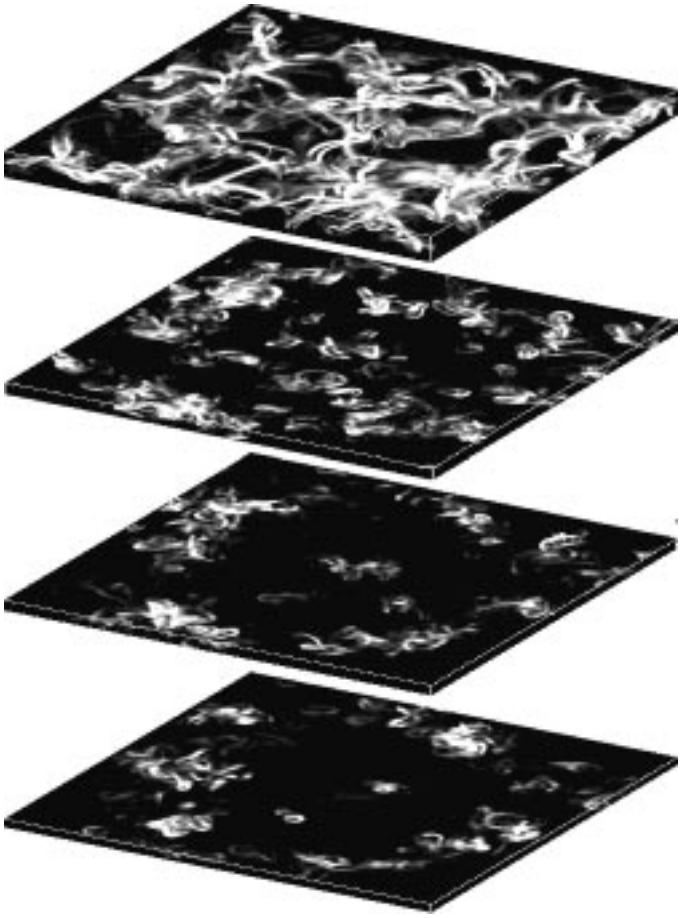

Figure 15. Horizontal slices showing vorticity at increasing depth. Vorticity is confined to the downdrafts, which outline the edges of the granules near the surface and the mesogranules deeper down.

4.1. DRIVING

Solar convection is non-locally driven from the extremely thin surface thermal boundary layer where radiative cooling produces the low entropy gas that forms the cores of the downdrafts in which most of the buoyancy work occurs (Figure 11). The entropy fluctuations are large at the surface and decrease with depth due to energy diffusion and entrainment and mixing in the downflows of overturning entropy neutral ascending fluid (Figure 12). In fact, most of the ascending fluid must turn over and head back down within a scale height in order to conserve mass in the stratified atmosphere. Thus the topology of the convection flows is controlled by mass conservation. It is somewhat like a fountain. What comes up in an ascending column flows out the sides and turns over within a scale height.

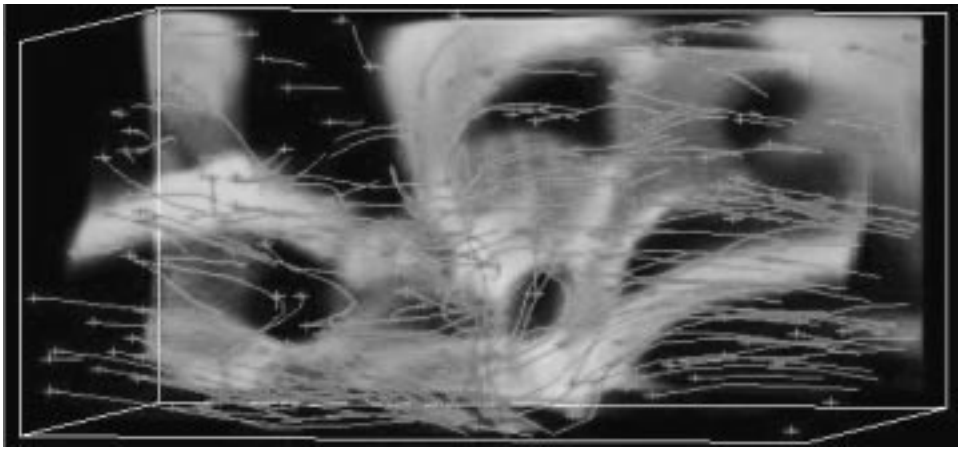

Figure 16. Image of magnetic field strength and superimposed magnetic field lines. Horizontal magnetic field is advected into the computational domain by fluid entering at the bottom.

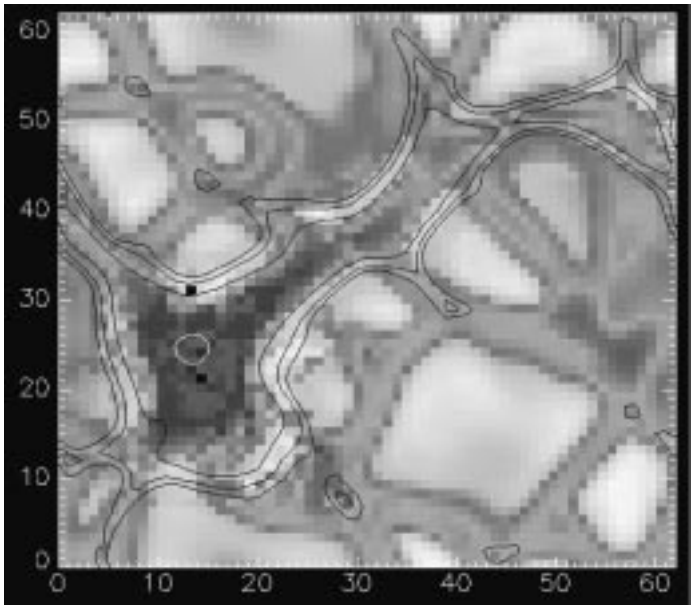

Figure 17. Granulation snapshot with superimposed magnetic field contours. A dark pore has formed in an intergranular lane where the field has been compressed to its maximum strength of about 2 kG. The domain is 6×6 Mm.

4.2. VORTICITY

Solar convection is characterized by turbulent downdrafts and relatively laminar upflows, not by a hierarchy of eddies (Figure 13). Upflows diverge which smooths out their fluctuations. Vorticity is produced at the edges of downflows by the mis-

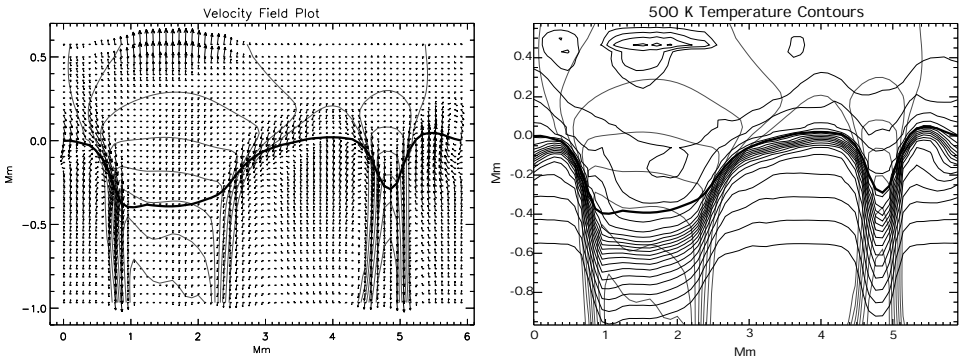

Figure 18. Slice through a pore (on the left side of each figure) and bright point (on the right side of each figure) showing the magnetic field contours and the fluid velocity vectors (*left*) and temperature contours (*right*). The heavy solid line is the optical depth unity surface. The convective velocity is not significantly depressed in the bright points but is in the pores. The downflow is concentrated in the boundary layer surrounding the pore. The $\tau = 1$ surface is depressed approximately the same in both pores and bright points, but the temperature is depressed much more in the pore than in the bright points due the inhibition of convective motions in the pores.

alignment of pressure and density gradients (baroclinic term) because of the entropy gradient and is strengthened by the compression of the descending fluid.

At the head of a descending downdraft there is a ring vortex with typically two (but sometimes more) vortex tubes connecting it back up to the surface (Figure 14). The horizontal scale of the upflows increases with depth, reaching mesogranule sizes by the bottom of our computational domain at 2.5 Mm below the surface. There is no indication of a distinct mesogranule size however. The downdrafts remain narrow and turbulent with increasing depth, outlining the edges of the mesogranules (Figure 15).

4.3. MAGNETO-CONVECTION

We have begun to investigate the properties of magneto-convection: the emergence of magnetic flux through the solar surface using a calculation where horizontal field is advected into the computational domain by fluid entering at the bottom (Figure 16), and the formation, evolution and destruction of pores using a calculation with an initially uniform, unipolar vertical magnetic field (Figure 17).

The magnetic field is swept into the downflows by the diverging upflows. In the bipolar case, advection and buoyancy stretch the field into loops. In both cases, where the surface field is strong the flux tubes become evacuated and radiation emerges from deeper in the Sun. Small strong field concentrations in the intergranular lanes, where the convective velocity is not suppressed, appear as bright points (Figure 18). Larger strong field concentrations, where the convective velocity is suppressed, appear as dark pores (Figure 18). The magnetic field significantly mod-

ifies the granulation pattern, producing smaller, more irregular granules (Bercik *et al.*, 1997).

5. Conclusions

We have used various, complementary, diagnostics to show the consistency between our model of convection and observations of the Sun. Weak lines are sensitive to the surface dynamics and temperature structure. p-mode frequencies depend on the mean atmospheric structure. p-mode driving is sensitive to the treatment of radiative cooling at the surface. The convection zone depth is controlled by the entropy jump and the thermal structure. Hence, we believe our physics is nearly right. The remaining differences between the synthetic and observed diagnostics are valuable clues to the still missing physics that needs to be included next, such as non-LTE radiation transfer and non-adiabatic wave propagation in an inhomogeneous medium. We are now beginning simulations on the larger scale of supergranulation to investigate the relation of granulation, mesogranulation and supergranulation, to provide a test bed for calibrating local helioseismic techniques, to investigate local small scale dynamo action and the role of magnetic fields in supergranulation.

Acknowledgements

This work was supported in part by NASA grants NAG 5-4031 and NAG 5-8053, NSF grants AST 9521785 and AST 9819799, and the Danish Research Foundation, through its establishment of the Theoretical Astrophysics Center. The calculations were performed at the National Center for Supercomputer Applications, which is supported by the National Science Foundation, at Michigan State University and at UNI•C, Denmark. This valuable support is greatly appreciated.

References

Basu, S. and Antia, H. M.: 1997, *Monthly Notices Royal Astron. Soc.* **287**, 189.

Bercik, D. J., Basu, S., Georgobiani, D., Nordlund, A., and Stein, R. F.: 1998, Solar Magneto-Convection. *Astronomical Society of the Pacific Conference Series*. San Francisco, p. CD568.

Boris, J. P.: 1989, in J. L. Lumley (ed.), *Whither Turbulence? Turbulence at the Crossroads*, Berlin, p. 344.

Brummell, N. H., Hurlburt, N. E., and Toomre, J.: 1996, *Astrophys. J.* **473**, 494.

Cattaneo, F.: 1999, *Astrophys. J.* **515**, L39.

Cattaneo, F., Brummell, N. H., Toomre, J., Malagoli, A., and Hurlburt, N. E.: 1991, *Astrophys. J.* **370**, 282.

Chan, K. L. and Sofia, S.: 1989, *Astrophys. J.* **336**, 1022.

Däppen, W., Mihalas, D., Hummer, D. G., and Mihalas, B. W.: 1988, *Astrophys. J.* **332**, 261.

Duvall, T. L., Jefferies, S. M., Harvey, J. W., Osaki, Y., and Pomerantz, M. A.: 1993, *Astrophys. J.* **410**, 829.
Elliott, J. R., Miesch, M. S., Toomre, J., Cluney, T. C., and Glatzmaier, G. A.: 1998, Turbulent Solar Convection and its Coupling with Rotation. *Structure and Dynamics of the Interior of the Sun and Sun-like Stars*, p. E168.
Freytag, B., Ludwig, H.-G., and Steffen, M.: 1996, *Astron. Astrophys.* **313**, 497.
Georgobiani, D., Kosovichev, A., Nigam, R. G., Stein, R. F., and Nordlund, A.: 2000, *Astrophys. J.* **530**, L139.
Hummer, D. G. and Mihalas, D.: 1988, *Astrophys. J.* **331**, 794.
Hurlburt, N. E., Matthews, P. C., and Proctor, M. R. E.: 1996, *Astrophys. J.* **457**, 933.
Kumar, P. and Basu, S.: 1999, *Astrophys. J.* **519**, 389.
Mihalas, D., Däppen, W., and Hummer, D. G.: 1988, *Astrophys. J.* **331**, 815.
Mihalas, D., Hummer, D. G., Mihalas, B. W., and Däppen, W.: 1990, *Astrophys. J.* **350**, 300.
Nigam, R., Kosovichev, A. G., Scherrer, P. H., and Schou, J.: 1998, *Astrophys. J.* **495**, L115.
Nordlund, Å.: 1982, *Astron. Astrophys.* **107**, 1.
Nordlund, Å.: 1985, *Solar Phys.* **100**, 209.
Nordlund, Å. and Stein, R. F.: 1989, in R. Rutten and G. Severino (eds.), *Solar and Stellar Granulation*, Kluwer Academic Publishers, Dordrecht, Holland, p. 453.
Nordlund, Å. and Stein, R. F.: 1990, *Computer Phys. Communications* **59**, 119.
Nordlund, Å. and Stein, R. F.: 1991, in L. Crivellari, I. Hubeny, and D. G. Hummer (eds.), *Stellar Atmospheres – Beyond Classical Models*, p. 263.
Nordlund, Å. and Stein, R. F.: 2000, *Astrophys. J.* (submitted).
Porter, D. H. and Woodward, P. R.: 1994, *Astrophys. J.* **93**, 309.
Porter, D. H., Pouguet, A., and Woodward, P. R.: 1992, *Phys. Rev. Lett.* **68**, 3156.
Rast, M. P. and Bogdan, T. J.: 1998, *Astrophys. J.* **496**, 527.
Roca Cortes, T., Montanes, P., Palle, P. L., Perez Hernandez, F., Jimenez, A., Regula, C., and the GOLF Team: 1999, in A. Jimenez, E. Guinan, and B. Montesinos (eds.), *Theory and Tests of Convective Energy Transport*, Vol. 173, *ASP Conf. Ser.*, p. 305.
Rogallo, R. S. and Moin, P.: 1984, *Ann. Rev. Fluid Mech.* **16**, 99.
Rosenthal, C. S., Christensen-Dalsgaard, J., Kosovichev, A. G., Nordlund, A. A., Reiter, J., Rhodes, J., Schou, E. J. J., Stein, R. F., and Trampedach, R.: 1998, in *SOHO 6/GONG 98: Structure and Dynamics of the Interior of the Sun and Sun-like Stars*, p. 521.
Rosenthal, C. S., Christensen-Dalsgaard, J., Nordlund, A., Stein, R. F., and Trampedach, R.: 1999, *Astron. Astrophys.* **351**, 689.
Stein, R. F. and Nordlund, Å: 1991, in D. Gough and J. Toomre (eds.), *Challenges to Theories of the Structure of Moderate Mass Stars*, Vol. 388 *Lecture Notes in Physics*, p. 195.
Stein, R. F. and Nordlund, Å.: 1998, *Astrophys. J.* **499**, 914.
Weiss, N. O., Brownjohn, D. P., Matthews, P. C., and Proctor, M. R. E.: 1996, *Monthly Notices Royal Astron. Soc.* **283**, 1153.